Journal of Energy Storage 179 (2026) 124007

Contents lists available at ScienceDirect

Journal of Energy Storage

journal homepage: www.elsevier.com/locate/est

Research papers

A flexible battery testing framework for accelerated research on photovoltaic-battery modules and a representative test time series

N'Danadje Bagnabana Konga [a,d,1], Sergey Shcherbachenko [a,1], Oleksandr Astakhov [a,*], Daniel Weigand [a], Ayouba Mahamane Abdoulkadri [d], Souley Kallo Moutari [e], Egbert Figgemeier [b,f], Christoph J. Brabec [a,c], Tsvetelina Merdzhanova [a]

[a] IMD3-Photovoltaics, Forschungszentrum Jülich GmbH, 52425, Jülich, Germany
[b] Forschungszentrum Jülich, Helmholtz Institute Münster, 48149, Jülich, Germany
[c] Friedrich-Alexander-Universität Erlangen-Nürnberg, 91058, Erlangen, Germany
[d] Faculty of Science and Techniques, Abdou Moumouni University, 10662, Niamey, Niger
[e] Ecole Normale Supérieure, Abdou Moumouni University, 10662, Niamey, Niger
[f] Faculty of Electrical Engineering and Information Technology, RWTH Aachen University, 52062, Aachen, Germany

A R T I C L E I N F O

Keywords:
Battery testing
Photovoltaic-battery modules
Photovoltaic battery
Versatile testing platform

A B S T R A C T

Surplus variable photovoltaic (PV) generation should be coupled to storage as close as possible to its point of generation to minimize grid stress and infrastructure expansion. This can be achieved by electrically coupling and physically integrating batteries at the PV module level, an approach that has been shown to be feasible but requires batteries adapted to PV-module-specific electrical and thermal operating conditions. In direct coupling, the battery current is set by the instantaneous interaction of PV and battery current-voltage characteristic, and the thermal conditions are dominated by the PV module temperature. Existing battery testing methods do not fully address this requirement space for early-stage laboratory cells. Here, we present a flexible battery testing framework that translates direct PV-battery coupling and PV-module thermal boundary conditions to laboratory-scale batteries. The platform combines a software-controlled PV emulator with a programmable thermal chamber to expose batteries to scaled PV I-V characteristics and PV-module-equivalent temperature profiles. It is demonstrated using a Li-ion cell under a representative seven-day PV profile for Freiburg, Germany. The emulator reproduces the target electrical conditions with cumulative charge and energy deviations of about 1.5%, while the tested configurations show PV-battery coupling efficiencies above 95%. The results demonstrate the platform's potential for screening laboratory-scale batteries by assessing relative PV-battery sizing, voltage matching, C-rate variation, state-of-charge swing, and direct-coupling behavior. The derived battery operating time series is also provided as a simplified proxy for preliminary screening on conventional battery cyclers.

1. Introduction

Photovoltaic (PV) deployment continues to outpace projections [1] and has the potential to become a dominant source of electricity [2]. However, further expansion is constrained by the intrinsic variability of PV generation and its temporal mismatch with electricity demand, which complicate large-scale adoption [3], particularly in weak-grid, off-grid, and mini-grid contexts [4]. Because of the relatively low capacity factor of PV, high annual PV shares require installed peak capacities well above average demand, leading to increasingly frequent periods of surplus generation. Energy storage therefore becomes a critical enabling component for PV-dominated electricity systems. Batteries are particularly well suited for short-term shifting of PV electricity over hours to days and are increasingly used to buffer variable renewable generation [5,6].

At high PV shares, the placement of storage in the PV energy-delivery chain becomes as important as storage type and capacity. Current PV-battery deployment is still largely dominated by centralized approaches at the transmission-grid or district level [5]. However, this approach is poorly aligned with the distributed nature of PV generation:

* Corresponding author.
E-mail address: o.astakhov@fz-juelich.de (O. Astakhov).
[1] Contributed equally to this work.

https://doi.org/10.1016/j.est.2026.124007
Received 23 March 2026; Received in revised form 25 June 2026; Accepted 31 July 2026
Available online 7 August 2026

surplus PV power must be aggregated from geographically dispersed generators [7] and transported through grid infrastructure that is already heavily utilized by routine electricity delivery [8–11]. Placing storage closer to the point of generation can reduce these power peaks before they enter downstream infrastructure. The most direct realization is PV-module-level or directly coupled PV-battery storage, where the battery captures variability at the origin of generation.

PV-module-level battery integration has two distinct but coupled aspects: electrical direct coupling and physical integration. Electrically, batteries are well suited for direct coupling to PV modules because, with appropriate voltage matching, high coupling efficiency can be achieved without maximum power point tracking or intermediate DC–DC conversion. The feasibility of such direct coupling has been demonstrated in theoretical and experimental studies [12–22]. At the module level, direct coupling captures PV variability at the earliest point in the energy-delivery chain, reduces output power peaks and the required power rating of downstream system components, while maintaining approximately the same energy output [23]. Physically, PV-module-level integration is feasible in terms of battery volume and mass [24,25] but it exposes the battery to PV-module-specific operating conditions. In particular, PV modules operate over a wide temperature range, typically from -10 °C to approximately $+70$ °C [24,26], while the battery simultaneously follows charge-discharge profiles dictated by irradiance, module temperature, state of charge, and load demand.

Mainstream batteries were not developed for this combined electrical and thermal stress profile. Viable PV-battery modules therefore require application-specific chemistries and cell designs, supported by validation methods that test new candidates under module-equivalent conditions before integration with actual PV devices. Such testing is challenging because PV-module operation exposes the battery to coupled irradiance-, temperature-, state-of-charge-, and load-dependent conditions.

Existing testing approaches leave this requirement space largely uncovered. Standard battery protocols use predefined current profiles and simplified thermal conditions, while PV laboratory tests are short and limited in irradiance and temperature range. Hardware-in-the-loop (HIL) and power hardware-in-the-loop (P-HIL) platforms for battery energy storage systems provide powerful tools for pack-, converter-, control-, and grid-level validation, but are typically designed for larger-scale BESS operation [27–31], not for early-stage cells or direct PV-battery coupling, where the operating point is set in real time by the interplay of PV and battery I—V characteristics. They also generally do not address PV-module thermal conditions. Full PV-battery prototype testing is more realistic, but resource-intensive, difficult to reproduce, and requires batteries large enough for practical module coupling. This creates a scaling gap with early-stage battery research, which is commonly performed on mAh- or sub-mAh-scale laboratory cells. Consequently, many emerging chemistries cannot be evaluated under PV-module-relevant conditions when optimization feedback is most needed.

Here, we address this gap by translating direct PV-battery coupling to laboratory battery scale. A software-controlled PV emulator reproduces scaled, field-relevant PV current–voltage characteristics from selected irradiance and module-temperature time series, while a programmable thermal chamber imposes the corresponding PV-module temperature profile. The emulated PV device can be defined from reported I—V parameters and thermal coefficients, enabling both commercial modules and novel laboratory PV devices to be represented. Combined with current and voltage scaling on the battery side, this allows batteries from mAh- or sub-mAh-scale laboratory formats to larger devices to be tested as virtual components of a target PV-battery module. In this way, batteries with different capacities can be exposed to operating conditions representative of real PV-battery prototype modules under field operation, without requiring electrical or physical integration with an actual PV device.

The approach enables reproducible test scenarios with user-defined PV module, climate, load, scaling, and duration, allowing systematic comparison of battery candidates under PV-integrated operating conditions. We present the platform architecture, validate its electrical and thermal response, and demonstrate its use with a single Li-ion cell under a representative PV-module operating scenario. The resulting current, voltage, state-of-charge, and charging-rate profiles are provided as a reduced proxy for preliminary testing on conventional battery cyclers, while full emulation remains necessary to capture real-time voltage-feedback effects in direct PV-battery coupling.

The paper is organized as follows. Section 1 presents the testing platform. Section 2 describes the measurement scenario. Section 3 introduces PV-battery sizing and voltage-profile matching for direct coupling. Sections 4 and 5 discuss the experimental results and evaluate the platform performance under representative operating conditions.

2. Novel versatile testing platform for PV-Battery systems

2.1. Testing platform structure and duty cycle

The diagram of the developed novel testing platform is shown in Fig. 1. It consists of four main components, including a thermal chamber, a source measure unit (SMU), a data logger, and a PV emulation code implemented on the computer. The battery under test is placed inside the custom-designed thermal chamber. The chamber features an automated cooling and heating system providing a controllable temperature setting ranging from -15 °C to 70 °C. During the measurement, a Keithley 2461 source measure unit (SMU) emulates the required PV current voltage characteristics according to the algorithm programmed with a Python script on the control PC. The SMU was operated in 4-wire remote-sense mode, so the voltage was controlled and measured at the battery terminals, minimizing the influence of ohmic voltage drops in the connection leads on the emulated PV-battery operating point. The PV emulator dynamically controls the SMU output to replicate the current–voltage (I—V) characteristics of a PV module under target irradiance and temperature conditions with accuracy on par with AAA class solar simulator [32]. A temperature sensor close to the battery measures its thermal state and transmits the signal to the proportional integral derivative (PID), which controls the heaters and coolers in the thermal chamber to smoothly reach the required battery temperature. The thermal data are continuously recorded by a HIOKi LR8450 data logger with high precision and a sampling rate of up to 1 ms.

Fig. 2 illustrates the duty cycle of the testing platform. The routine starts with connecting the devices and is followed by the thermal chamber's temperature stabilization. Once the initial desired temperature is reached, the emulator updates the PV I—V parameters (irradiance, temperature) and estimates the initial operating point. The SMU then performs the PV emulation phase, during which it continuously adjusts the output current and voltage in accordance with the emulated

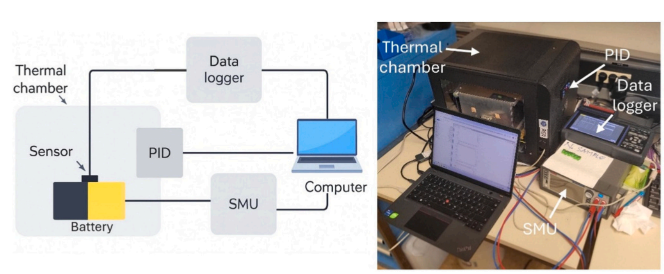

Fig. 1. Novel testing platform for PV–battery systems. The platform comprises a source measure unit (SMU) controlled by an emulation script on the computer that acts as the PV module to charge the battery placed inside the thermal chamber. The proportional integral derivative (PID) controller regulates the heaters and coolers in the thermal chamber to smoothly reach the set temperature. The data logger records the battery temperature, while the SMU provides the charging data.

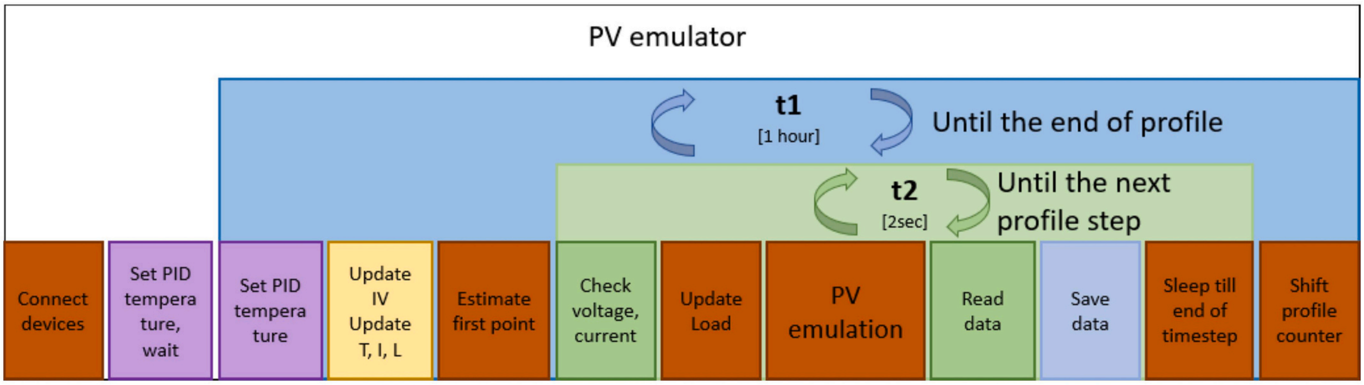

Fig. 2. Block diagram of the duty cycle.

solar profile. Simultaneously, voltage, current, and temperature data are acquired, stored, and updated in real time. Each emulation step is repeated within a one-hour cycle until the complete PV charging profile is executed. A more detailed description of the PV emulator will be provided in the following section.

2.2. PV emulator

The PV emulator used in this study is a Python-based software emulator built in-house. The emulator, shown in Fig. 3, can precisely mimic the behavior of a photovoltaic cell or module under various operating conditions and runs on off-the-shelf lab hardware. The emulation algorithm is based on a solution previously developed at the institute for testing electrochemical (EC) devices. The initial algorithm starts by communicating with the source measure unit (SMU) to measure the current and voltage in the system, also referred to as the working point (WP). Based on this working point and a predefined set point $(V_{load0}I_{load0})$, the IV curve of the EC cell is approximated using a straight line. The resistance associated with this linear approximation is calculated as:

$$R = \frac{V_{now} - V_{load0}}{I_{now} - I_{load0}} \tag{1}$$

The algorithm then determines the intersection between the preloaded PV IV curve and the estimated EC cell IV curve by solving for the voltage at which the following equation equals zero:

$$VI(Voltage) - \frac{Voltage - V_{load0}}{R} = 0 \tag{2}$$

If the difference between the current WP and the desired WP exceeds a predefined dead zone, the SMU is instructed to set the voltage to V_{obj}, and the current limit to I_{obj}.

This iterative approach gradually aligns the working point with the IV curve of the PV module and maintains it there. An optimal choice of (V_{load0}, I_{load0}) further enhances the convergence speed of the algorithm by improving the accuracy of the linear approximation of the EC cell IV curve. However, when applied to battery systems, the use of a single fixed set point $(V_{load0}I_{load0})$ is no longer optimal, since the battery IV curve continuously shifts during the charging process. To address this limitation, several modifications were implemented to adapt the algorithm for battery applications. Given that the battery IV curve is typically a steep line offset from the origin by the open-circuit voltage, the selected current range plays a critical role in the accuracy of the measurements. Consequently, the algorithm requires a predefined current value I_{bat}, which ensures that the battery IV characteristics are measured under suitable conditions. In the new adapted algorithm approach, the SMU voltage is first set to a maximum value V_{max}, defined as a safety parameter in the code, while the current limit is set to I_{bat}, ensuring that the SMU operates in current-limited mode. The resulting voltage and current are recorded as $V_{now}$and I_{now}. A second operating point $(V_{load1}I_{load1})$ is then obtained by repeating the measurement with a reduced current limit of $I_{bat}/2$. Using these two points, the internal resistance of the battery is calculated as:

$$R = \frac{V_{now} - V_{load1}}{I_{now} - I_{load1}} \tag{3}$$

Instead of relying on a predefined $V_{load0}$to compute the resistance, the algorithm rather uses the measured working point and the calculated resistance to determine V_{load0} according to:

$$V_{load0} = V_{now} - I_{now}R \qquad for\ I_{load0} = 0 \tag{4}$$

The emulator response time of approximately 1 s represents the readjustment time after a new PV I—V curve is imposed and defines the practical time resolution of the present setup. The platform is therefore intended for long-duration PV-battery operating profiles with discrete irradiance and temperature updates, rather than for studying high-frequency oscillations or short transients with sub-second characteristic periods. For profile steps of approximately 2 min or longer, the readjustment time corresponds to less than 1% of the step duration and is not expected to significantly affect cumulative coupling or energy balance over the measurement period.

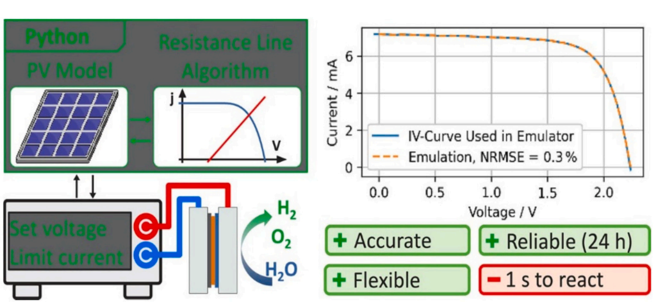

Fig. 3. Schematic illustration of the software-based PV emulator developed by [32]. The emulator uses Python-based software and off-the-shelf laboratory equipment to accurately replicate the current-voltage (IV) curve of a photovoltaic cell or module under various operating conditions. In this work, a Keithley 2461 source measure unit (SMU) is used as the core device for reproducing the PV I—V curves.

2.3. Evaluation of the thermal chamber's temperature emulation capability

The thermal chamber (Fig. 4) developed for the testing platform is designed to mimic the temperature conditions experienced by a battery. The temperature regulation is achieved using a Peltier element that operates in both heating and cooling modes. Coupled to the chamber and a PID controller, it allows for the application of controlled

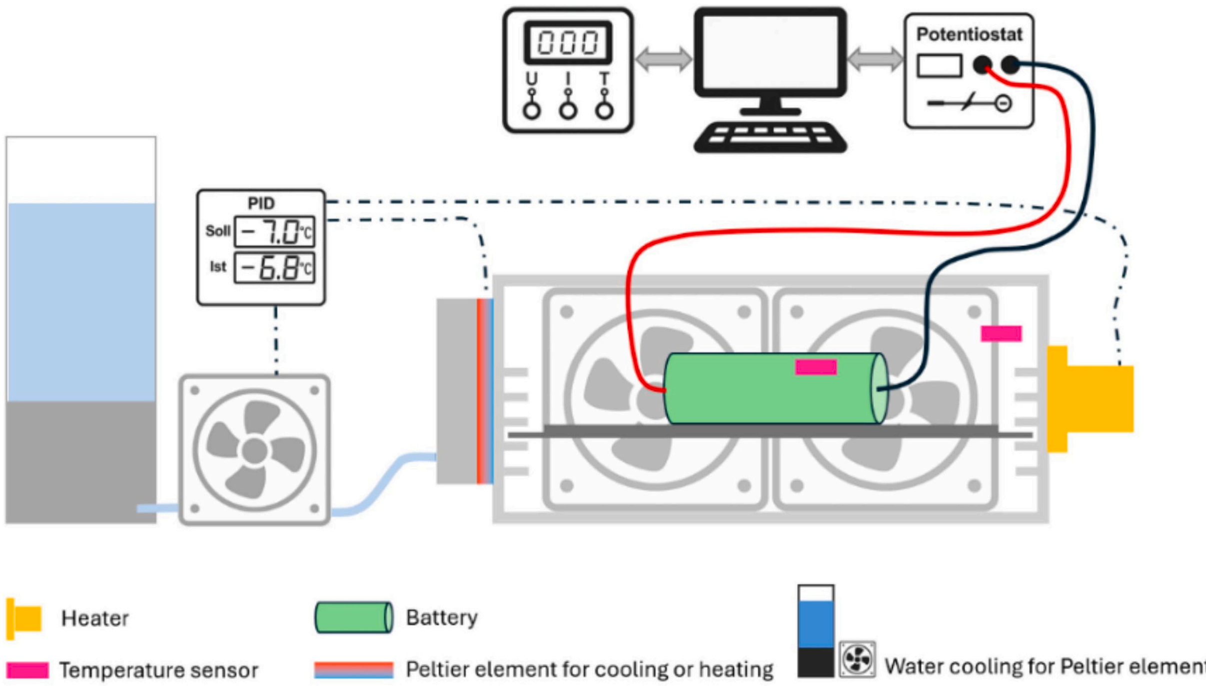

Fig. 4. Thermal chamber design and structure.

temperature profiles. To dissipate the heat generated on the hot side of the Peltier element, a water-cooling system, assisted by a fan, is integrated. The battery temperature is measured using a temperature sensor placed directly on it. The measurement is transmitted to the PID controller, which adjusts the power applied to the Peltier element in real time to maintain the set temperature. An auxiliary heater is also integrated to extend the thermal operating range and improve stability during the heating phases.

To evaluate the thermal response and regulation capacity of the developed thermal chamber, a tracking temperature experiment was performed. The experiment consisted of applying a stepwise setpoint temperature profile on the controller, increasing from −10 °C up to 70 °C and then gradually decreasing down to −20 °C, while measuring the temperature on the internal mounting base of the thermal chamber.

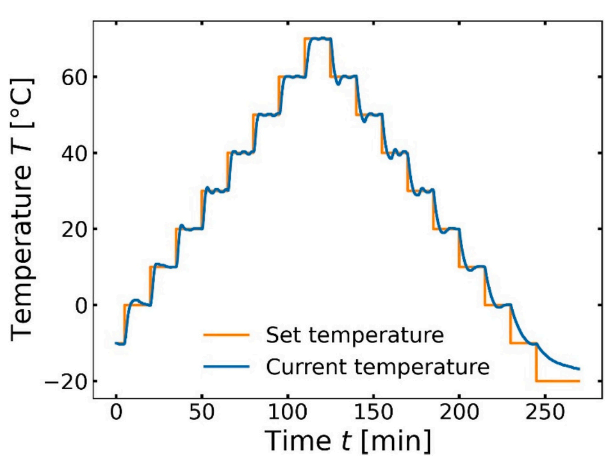

Fig. 5. Evolution of the temperature during the thermal chamber operation. The orange curve represents the set temperature, while the blue curve shows the measured temperature. The set temperature follows a stepwise profile starting from −10 °C up to 70 °C and back down to −20 °C. (For interpretation of the references to colour in this figure legend, the reader is referred to the web version of this article.)

Fig. 5 shows the thermal behavior of the chamber during this experiment. The orange curve represents the setpoint temperature, while the blue curve corresponds to the temperature measured inside the compartment. Over the entire range, the measured temperature follows the set temperature closely, reflecting the good dynamic response of the control system. Transient overshoots are observed at each plateau transition; however, the maximum overshoot remains limited to approximately ± 1 °C. The chamber heats from 20 °C to 70 °C in 16.19 min and cools from 70 °C to 20 °C in 15.98 min, showing similar performance for heat injection and extraction in that temperature range (heating rate $\approx$ 3.09 °C /min, cooling rate $\approx$ 3.13 °C /min). Cooling from 20 °C down to 0 °C takes 10.18 min, resulting in a cooling rate of 1.96 °C/min. Below 0 °C, the cooling capability decreases substantially and takes a longer time, with approximately 21.9 min to cool down from 0 °C to −15 °C. Overall, the thermal chamber provides stable and accurate thermal behavior, ensuring controlled experimental conditions for the time scales typical of battery testing.

In the present configuration, the temperature is controlled and measured at the battery surface or mounting position; battery core temperature and internal thermal gradients are not directly measured, so the imposed profile should be interpreted as a controlled module-equivalent boundary condition rather than a full thermal model of an integrated battery. Note that the PID-controlled chamber also compensates possible internal battery heating at high charge or discharge rates in order to maintain the prescribed PV-module temperature profile. The experiment therefore approximates operation under a PV-module thermal boundary condition; however, precise assessment of battery self-heating, internal temperature gradients, and module-battery heat exchange would require physical PV-battery integration under field conditions.

3. Measurement scenario

3.1. Irradiance, temperature, load power profiles

To demonstrate the practical application, functionality, and performance of the developed platform, the latter was experimentally tested under realistic operating conditions of a PV module installed in the region of Freiburg, Germany. The test scenario was generated using a typical meteorological year (TMY) time series of irradiance and ambient temperature obtained from the Photovoltaic Geographical Information System (PVGIS), for the exact location at latitude 47.997° N and longitude 7.868° E. One straightforward limitation of this time series is the duration of one year, which is impractical in most cases. In order to accelerate the test while maintaining a relevant variety of operating conditions and satisfactory representativeness of the year, we selected a subset of days distributed over the annual TMY dataset, resulting in a representative seven-day time series. Hourly plane-of-array irradiance and module temperature were computed from a Typical Meteorological Year (TMY) dataset at optimal fixed-tilt orientation. The corresponding maximum-power-point energy was accumulated into a two-dimensional histogram over temperature and irradiance bins, forming an energy distribution map that characterizes how annual energy output is partitioned across operating conditions. A set of N equally spaced days (spaced $\lfloor 365/N \rfloor$ days apart) was then slid across the year by varying the start day offset, and for each offset the normalized energy distribution of the selected days was compared to the full-year distribution via root-mean-square difference, selecting the offset that minimizes this difference and yields a compact N-day profile faithfully reproducing the annual operating conditions. The detailed selection procedure and the complete hourly input dataset, including meteorological data, POA irradiance, module temperature, and MPP power, are provided in the Supplementary Information.

The meteorological data were used to calculate the plane-of-array (PoA) irradiance and the PV module temperature using the pvlib library implemented in Python. The PoA irradiance was obtained by transposing the measured global horizontal irradiance (GHI), direct normal irradiance (DNI), and diffuse horizontal irradiance (DHI) onto the tilted module plane. The PV module temperature was then estimated using the Faiman temperature model, accounting for ambient air temperature, wind speed, and PoA irradiance [33,34]. The resulting PoA irradiance and module temperature were used to calculate the time series of PV I-V characteristics based on the CEC single-diode model, and the module temperature is used as a setting for the thermal chamber to represent thermal conditions of the PV module for the battery. The CEC single-diode model provides a standard and sufficiently accurate description for the dominant energy-generating irradiance range considered here; however, low-irradiance conditions may introduce larger uncertainty due to shunt-related effects, and measured I-V curves or more advanced PV models can be used as emulator input when higher low-light accuracy is required. The load profile used in this study is a representative household demand profile scaled so that its total energy demand over the selected period matches the total PV energy produced at the module maximum power point. As a result, the load demand varies proportionally with the emulated PV production, increasing during periods of high PV output and decreasing when the PV generation is low, thereby ensuring a realistic interaction between the load profile and the PV emulation.

Fig. 6 presents the time series with all the realistic profiles used for the measurements. The plane of array irradiation profile received by the PV module (Fig. 6a) reveals significant variations in solar irradiance, ranging from very low irradiance days to peaks reaching nearly 1000 W/m^2. The module temperature (Fig. 6b) follows a similar trend, with increases during irradiance peaks and decreases at night or during overcast days. In the case of PV module integration, the battery experiences a thermal profile very close to the module temperature. Therefore, the battery temperature is assumed to be identical to that of the photovoltaic module during realistic measurements. Fig. 6c illustrates the load profile used during the measurements. This is a standard daily profile of household consumption applied identically over the study period.

3.2. IV curves generation for PV emulator

To provide input IV time series for the PV emulator, a complete set of I—V curves was generated using the 7-day irradiance and temperature profiles derived from the processed climatic dataset (Fig. 6). In this work, we emulated the IV curves from the Neostar 3N54 AIKO-A-MCE54Mw 495 W module. For each hour and over the 7-day period of measurement, the irradiance and temperature values were processed to generate the corresponding hourly PV IV curve. The resulting set of IV curves (Fig. 7) reflects the hourly electrical response of the PV module over the 7-day period of measurement under the considered climatic

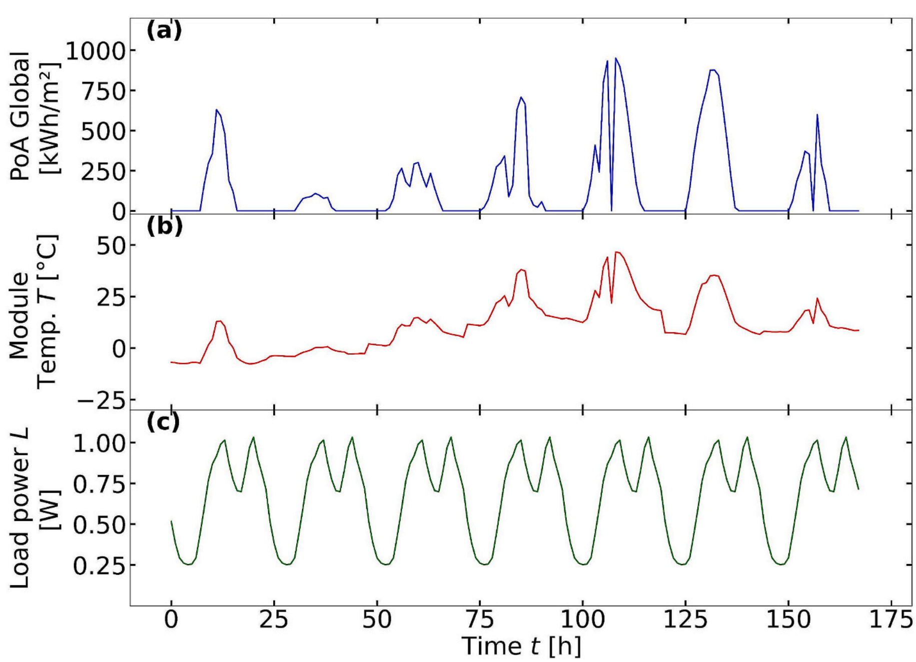

Fig. 6. Plots (a) and (b) show the plane-of-array (PoA) irradiance received by the PV module and the corresponding module temperature profile, respectively. These profiles were obtained by rescaling several years of real meteorological data from Freiburg, Germany, to a representative seven-day sequence. Plot (c) illustrates the standard daily household load profile over the same seven-day period, scaled to match the total PV energy produced at the module's maximum power point (MPP).

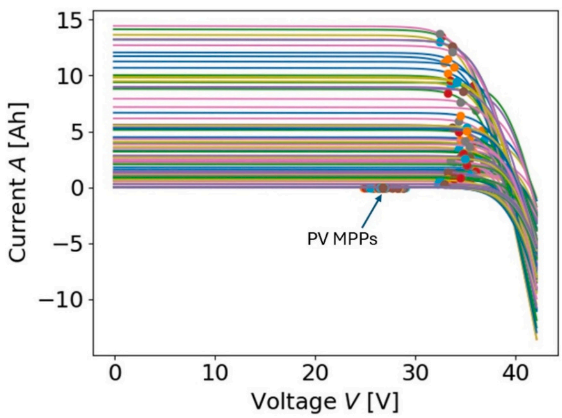

Fig. 7. Hourly current–voltage (I—V) characteristics of a photovoltaic (PV) module generated over the representative seven-day period using the plane-of-array (PoA) irradiance and module temperature profiles shown in Fig. 6. The I-V curves form the dataset used as input for the PV emulator.

conditions.

4. PV–Battery unit sizing and profile matching

A Li-ion battery (ref:ANR26650m1B) with 3.3 V nominal voltage and 2 to 3.6 V operation voltage range was used for testing in our study. To safely charge the battery with the PV module, direct coupling requires careful component matching. Particularly, sizing and voltage matching are important. With PV-emulator, the matching and sizing can be performed without the physical connection of battery cells in series or parallel. The set of PV IVs can be scaled in terms of both current and voltage to emulate proper coupling conditions. To guarantee high efficiency of a PV-battery module the battery operating voltage range must be close to the maximum power point (MPP) of the PV module [12]. Three PV-battery combinations with different battery sizes including a 1, 2 and 4-h batteries were explored. The size of the battery is defined based on how many hours it takes to charge with nominal PV power under standard test conditions. The term “1-h battery” denotes a battery capacity sized relative to the PV system such that it can be fully charged within one hour under standard PV operating conditions. For example, a 1 kWp PV system paired with a 1-h battery corresponds to a battery capacity of 1 kWh. This time-based measure of PV–battery scaling can be adjusted by changing either the PV nominal capacity or the battery capacity. Unlike conventional practice, where the battery is added to an existing PV system and scaled to its nominal power, the proposed testing platform provides full flexibility on the PV side. As a result, batteries at any research scale can be evaluated in the context of full-scale PV systems based on the target PV technology. The PV module sizing is done by the scaling of the current and voltage of the PV module to match the characteristics of the battery. For each battery size, the procedure consisted of summing all PV power curves within the generated timeseries (corresponding to IV curves in Fig. 7). This summation results in the PV energy curve representing the dependence of the PV output energy on the operating voltage over the entire period of operation. The IV set presented in Fig. 7 results in the energy-voltage curves shown in a solid blue line in Fig. 8a. To maximize the coupling of PV energy to the battery, the battery operating voltage should be aligned as closely as possible with the PV maximum power region. An exact solution to the coupling problem is impractical for real battery devices due to the complex dependence of battery voltage on charge history, thermal history, state of charge, and state of health. From the PV perspective, a fully rigorous solution is not required, as real ambient conditions are never reproduced exactly. Instead, a practical approach relies on approximate optimization using representative time series. The starting hypothesis for this optimization is to ensure that the battery voltage operating range covers the region of maximum PV energy output, as illustrated in Fig. 8a. Here the dotted blue lines indicate the minimum and maximum battery voltage, respectively, 2.8 V and 3.55 V chosen for the matching.

The PV energy available at the minimum and maximum battery voltages, corresponding to the intersection points between the PV energy curve and the battery voltage limits, therefore represents key energy levels that characterize the effectiveness of the PV–battery coupling. Therefore, the optimization aims to maximize the PV energy at these two intersection points. This is achieved by progressively shifting the PV energy curve so that both intersection energies are positioned as close as possible to the maximum of the PV energy curve, while remaining high and well balanced.

To test the initial hypothesis of optimal matching presented in Fig. 8a, we defined an alternative set of operating conditions and performed experiments with the battery voltage range shifted away from the center of the PV maximum power region toward lower voltages (2.8–3.55 V), as shown in Fig. 8b.

5. Results and discussion

5.1. Cycling of the PV-battery unit under realistic irradiance and temperature scenarios

The results from the measurements performed by subjecting the

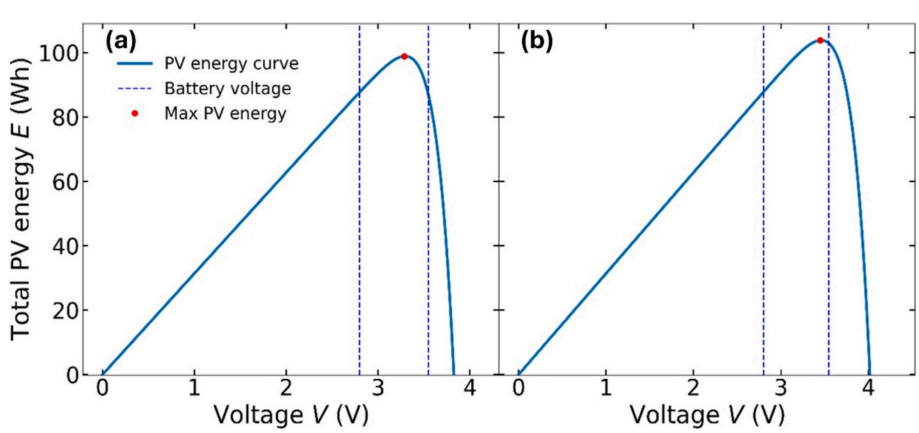

Fig. 8. Profile matching between the PV module and a 2-h battery. Plot (a) shows the profile matching between the PV module and the 2-h battery for the safe voltage matching range (2.8 to 3.55 V), plot (b) shows the profile matching with 5% deviation applied on the safe matching voltage range. The blue dashed lines indicate the battery voltage range used for matching. The solid blue line represents the sum of all the PV IV curves generated in Fig. 7. (For interpretation of the references to colour in this figure legend, the reader is referred to the web version of this article.)

battery to the conditions of a real PV module under realistic temperature and irradiance scenarios are shown in Fig. 9. Results are presented for emulation of three systems with different PV-battery scaling equivalent to PV systems with 1, 2, and 4-hour batteries. Fig. 9a illustrates an example of the operating power of the system elements in a 1 h battery system. Maximum attainable PV power (PV MPP) and operating power of PV, battery, and load are presented for the experiment emulating 7 days of operation. The power profiles in 2 and 4-hour batteries exhibit similar trends and are presented in Supplementary fig. 1.

The results indicate that the PV module operates very close to its MPP over the duration of the experiment, even in the absence of an MPP tracking device. The battery absorbs the surplus energy (positive values) and delivers it to the load during periods of deficit, which is reflected by negative values in the battery power. The PV power coupling factors in three PV modules with 1, 2, and 4-h batteries are shown in Fig. 9b, c, d. The coupling factor (C) is obtained by the ratio between the power delivered by the PV module at its working point (P_{WP}) and the maximum power (P_{MPP}) available under the same irradiance, and it is given by $C = P_{WP}/P_{MPP} = V_{WP}I_{WP}/V_{MPP}I_{MPP}$. The periods of dawn, night, and dusk, characterized by minimum to no irradiation, are excluded for the clarity of presentation. Overall, the coupling between the battery and the module is high and often greater than 90% for the different battery sizes tested, which reflects a good match between the PV module operating voltage and the battery voltage. The coupling factor is generally very high and close to 100% during the periods of major PV generation in the day, explained by the proper alignment between the PV maximum power point voltage (V_{mpp}) and the battery operating voltage. At the beginning and the end of the days and during dense cloudy conditions, the coupling factor can fall below 80% due to significant deviation of the PV working point from the battery voltage. These drops are marginal to the energy coupling as the periods of low irradiance have little impact on the resulting energy yield. Overall, over the 7-day period of measurement, a good performance of the system is observed with a cumulative coupling of 95.04%, 95.17%, and 96.75% reached, respectively, at the end of the experiment for the 1, 2, and 4-hour batteries. This is a good result comparable to the best MPP solutions in the literature, with an MPP power efficiency of 93–96% [35,36].

According to the cumulative coupling (energy coupling) results we can see that larger batteries promote coupling. This improvement can be attributed to reduced magnitude and frequency of voltage variations in the case of larger battery. Fig. 10 shows the battery voltage and current for the three battery sizes tested. Daily, in all three cases, alternating battery charging and discharging phases are observed. At the beginning of the day, the gradual increase in solar irradiance leads to a simultaneous increase in the battery voltage and current, reflecting the charging phase. On the other hand, at the end of the day, the decrease in photovoltaic production causes a drop in these electrical parameters, marking the transition to the battery discharging phase. The amplitude of variation of these two electrical parameters is a function of the battery size. We observe a gradual decrease in the amplitude of voltage and current variations as the battery size increases. For the 1-hour battery, there are significant voltage variations associated with high current peaks of up to 0.6C, while the 2 and 4-hour batteries exhibit more moderate voltage and current amplitudes of up to 0.3C for the 2-hour battery and up to 0.15C for the 4-hour battery. A higher current rate leads to an increase in the overpotential, which will increase the voltage range and reduce battery round-trip efficiency. A wider battery voltage range results in more frequent and stronger deviations of the operating voltage from the MPP voltage of the PV module, thereby reducing the coupling factor. Therefore, in the direct coupling approach, stable high coupling is easier to achieve with a larger battery of 2-hour and beyond.

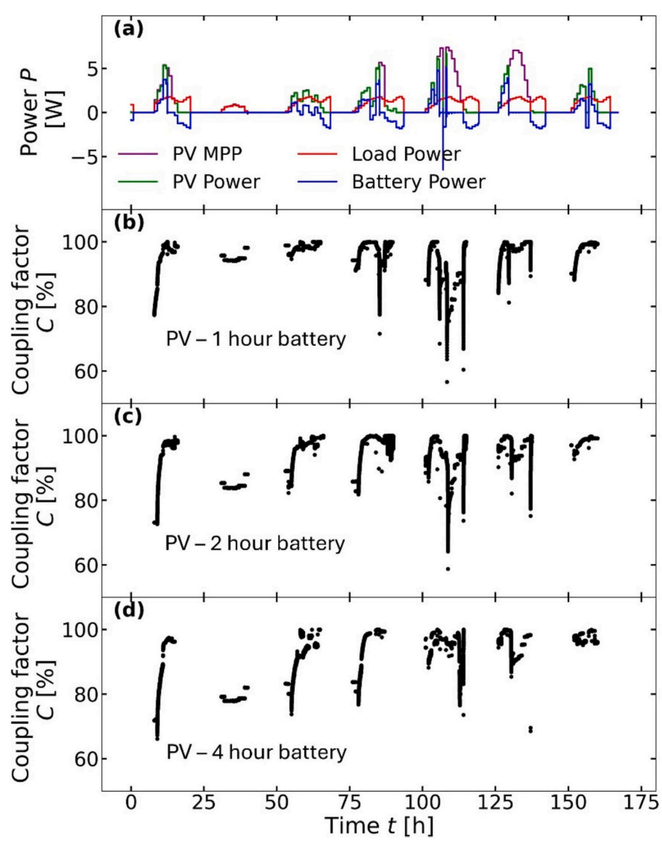

Fig. 9. (a) Realistic cycling measurement with a 1-hour battery. The plot (a) shows the power distribution in the PV–battery unit over the 7-day measurement period. The coupling factor between the PV module and the battery as a function of time is presented for (b) a 1-hour battery, (c) a 2-hour battery, and (d) a 4-hour battery.

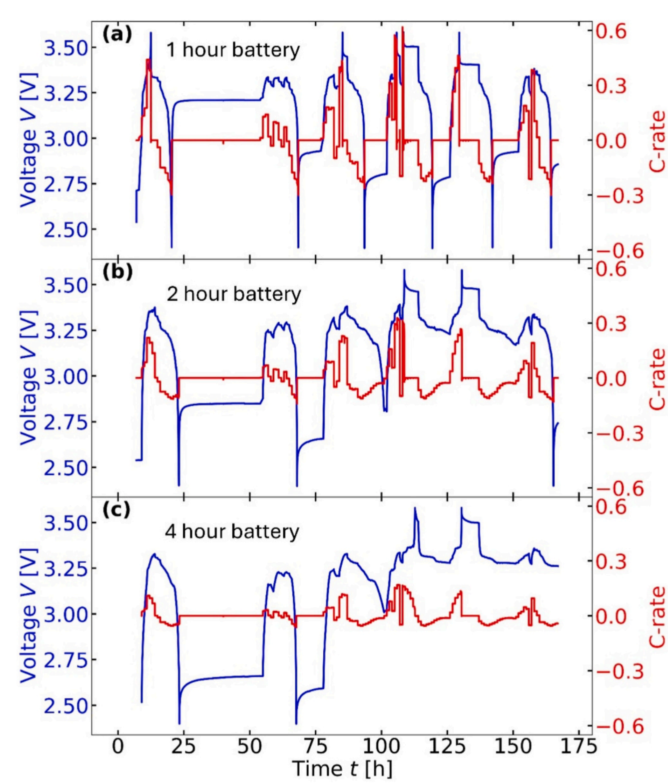

Fig. 10. Battery voltage (blue) and current (red) against time over the 7-day measurement period for (a) 1-hour battery, (b) 2-hour battery, (c) 4-hour battery. (For interpretation of the references to colour in this figure legend, the reader is referred to the web version of this article.)

The evolution of the battery SOC for the three battery sizes is shown in Fig. 11. The SOC is obtained by coulomb counting using the expression SOC = 100 × (∫Idt)/2.5. The charged/discharged capacity (∫Idt) in Ah is divided by the nominal full capacity of 2.5 Ah and multiplied by 100 to obtain the SOC in %. Daily, as it can be seen in Fig. 11, the 1-h battery (Fig. 11a), which is subjected to a higher current, is mostly cycled from a low SOC to a high SOC compared to the others. We note an almost total absence of the battery charging phase during the second day for all three cases. Fig. 10 indeed shows that, during this period, the battery voltage and current increased only slightly for the former and remained at zero for the latter for all three cases. This behavior is explained by the low irradiance during this period as demonstrated in Fig. 6a. Therefore, the PV production is insufficient to simultaneously charge the battery and supply the load. The PV production was also not sufficient to charge the 4-hour battery during the third day. As observed, a smaller battery undergoes more frequent cycling, operating over nearly its entire capacity range. Although this allows for a higher utilization of the available capacity and reflects typical household usage patterns, this long-term situation accentuates electrochemical ageing phenomena and therefore accelerates battery degradation. The combined effect of C-rate, SOC swing, and PV-module temperature profile is an important degradation-relevant condition that can be addressed with the present platform in future dedicated ageing studies. The present platform is focused on single-cell testing; pack-level effects such as cell balancing or pack thermal management require future platform extensions. Optimal battery size selection requires a compromise between maximizing battery capacity and durability. From an energy efficiency point of view, frequent and long periods of maximum or minimum charge state indicate a loss of available energy during periods of high generation and an inability to supply the load during battery-driven operation when the battery capacity is insufficient. From this perspective, the 4-h battery represents very reliable short-duration storage, providing sufficient energy to shift from surplus to deficit periods in most cases.

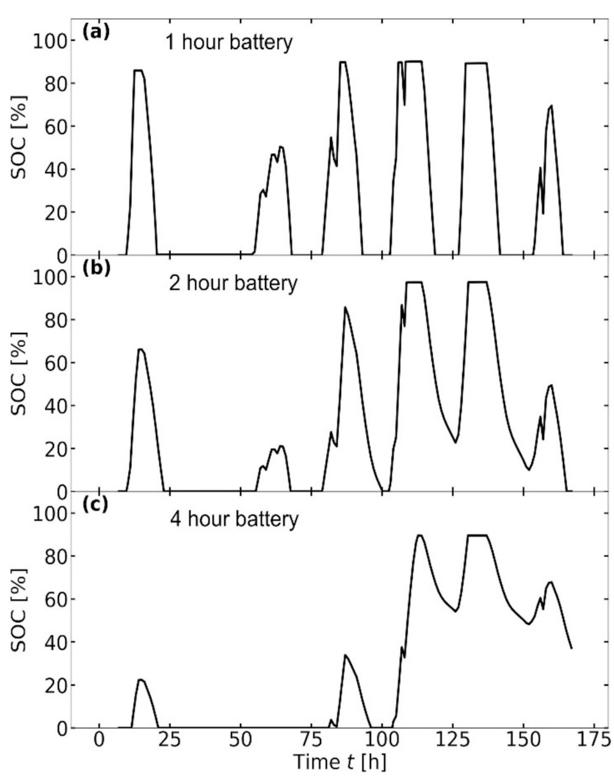

Fig. 11. Battery state of charge (SOC) over the 7-day measurement period for (a) 1-h battery, (b) 2-h battery, (c) 4-h battery. The SOC was obtained by dividing the charged/discharged capacity by the battery's nominal full capacity.

The time series of battery operating conditions obtained from the PV-driven test shown in Fig. 11 is provided in tabular form in the Supplementary Material. This dataset can be used as a practical proxy for preliminary evaluation and comparative screening of battery chemistries without PV emulation, and can be implemented on conventional battery cyclers to approximate PV-battery operating conditions. This time series should be interpreted as a simplified proxy: while it enables cycler-based screening, it does not reproduce the real-time PV-battery voltage feedback and I—V operating-point formation captured by the full emulation platform.

In the previous section (Fig. 8 and related discussion), we proposed a straightforward approach for PV–battery energy coupling based on aligning the battery operating voltage range with the region of maximum PV energy output. This hypothesis requires experimental verification. To this end, two experiments were conducted using a 2-hour battery configuration. In the first case, the battery voltage range was aligned to fully cover the PV maximum energy region. In the second case, a 5% voltage shift was introduced, moving the battery operating range toward the lower-voltage shoulder of the PV energy peak (see Fig. 8) as a small but noticeable perturbation. The purpose of this shift was to test whether the initial matching criterion, based on aligning the battery operating voltage range with the maximum PV energy region, indeed provides the best coupling. The shifted case therefore represents an alternative PV-battery matching configuration with displaced voltage alignment.

Fig. 12 shows the evolution of the energy coupling over the period of measurement for the two matching conditions previously mentioned. The reference matching is shown in red, while the blue curve shows the case where a 5% deviation is applied to the reference matching voltage range. For both cases, a noticeable degradation of the energy coupling is observed at the beginning of the measurement, where the coupling dropped to 89% and 73%, respectively, for the shifted and the reference matching case. This results from the low irradiance observed during this period, as it corresponds to early hours. As time progresses, the coupling energy in both cases improves and stays above 92% over the rest of the measurement period. Overall, both cases exhibit high energy coupling in the end with a respective cumulative energy coupling of 95.17% and 97.06% for the reference and shifted case. The shifted case shows that the initial maximum-energy matching criterion does not necessarily define a unique optimum. In the tested scenario, cumulative energy coupling remained high for both configurations and was slightly higher for the shifted voltage alignment. Overall, the result suggests that the tested 5% voltage shift had only a limited effect on cumulative coupling in this specific scenario. At the same time, the method of optimal coupling is yet to be developed, which will require more intensive experiments to acquire more statistics. Overall, we observed that, from an energy perspective, direct coupling between the PV module and the

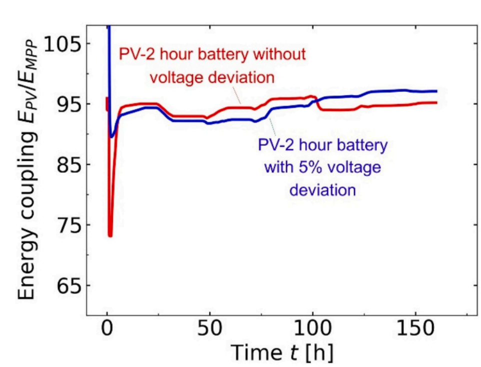

Fig. 12. Energy coupling over time comparison for the PV-2-h battery unit with 5% deviation applied on the reference matching voltage range (blue curve) and without deviation (red curve). (For interpretation of the references to colour in this figure legend, the reader is referred to the web version of this article.)

battery provides high coupling in a wide range of voltage and capacity matching scenarios, indicating that direct coupling can remain effective across the tested voltage and capacity matching scenarios.

5.2. Effect of battery size on PV utilization

A set of analyses was conducted to assess the effect of battery presence and size on the performance of a PV–battery system in terms of effective utilization of the PV generation potential. The analysis focuses on quantifying how many PV peak hours were effectively absorbed by the load (delivered to the load) at different battery sizes. For each configuration, namely, no battery, and batteries with 1, 2, and 4-hour capacities, the energy delivered to the load was calculated by integrating the load power over time as $E = \int P dt$. The energy obtained was then normalized with respect to the PV peak power. The result, expressed in hours, corresponds to the equivalent number of PV peak-power hours delivered to the load.

The results obtained from this analysis are illustrated in Fig. 13. In this figure, the yellow histogram bar represents the module's MPP power, while the red, blue, and green bars show the equivalent hours of PV peak generation absorbed respectively for the 1, 2 and 4-h battery. The purple bar corresponds to the configuration without a battery. The configuration without a battery means that the energy produced by the PV module is transferred directly to the load. The introduction of a battery, regardless of its size, has a significant impact on the number of hours the PV peak generation is collected. The battery extends the number of equivalent hours during which the peak PV generation is collected, i.e., the degree of utilization of PV energy. With a battery, the system can collect more than 13 h of peak PV generation, compared to only around 6.5 h without a battery. Indeed, the battery acts as an energy buffer, absorbing excess energy during periods of intense sunlight and releasing this energy during periods of reduced irradiance. By comparing different battery sizes, the 4-hour battery shows a slightly better ability to collect energy, however the gain is marginal as compared to the 2-hour battery. Both histograms (blue and green) for 2-hour and 4-hour batteries nearly overlap for most relative power levels, indicating that increasing the storage capacity beyond 2-hour does not significantly improve PV utilization in the studied case. While the optimal battery size depends on system purpose, installation location, and load profile, the 2-hour battery provides a good compromise for the selected household-load scenario. Other load profiles, including industrial demand or EV charging, require future dedicated studies enabled by the platform.

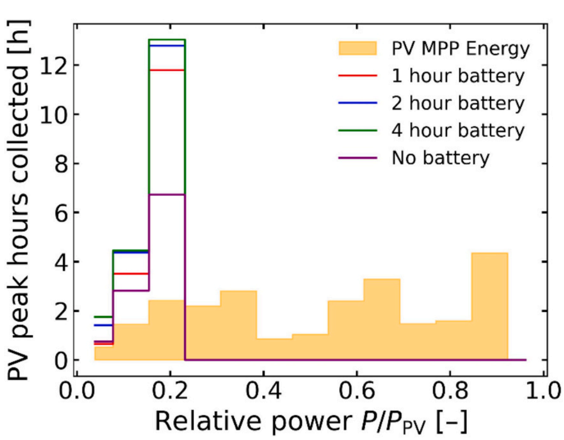

Fig. 13. Impact of battery presence and size on PV utilization. In yellow is the energy at the PV module maximum power point. The pink histogram bar represents the equivalent hours of PV peak generation collected with a 1-hour battery, the blue with a 2-hour battery, the green with a 4-hour battery, and the red shows the case without a battery. In the no-battery case, the PV production is considered directly delivered to the load. (For interpretation of the references to colour in this figure legend, the reader is referred to the web version of this article.)

The energy balance and the role of the battery size is analyzed further by the energy profiles for different components of the PV-battery unit. Fig. 14 shows the energy profiles evolution in the PV-battery unit for (a) 1-hour battery, (b) 2-hour battery and (c) 4-hour battery. The green curve indicates the ideal energy that would be harvested if the PV always operated at its MPP, the red curve shows the energy generated by the PV module (E_{PV}), in blue is shown the energy delivered to the load (E_{Load}) while in black is the battery energy ($E_{Battery}$). In all three cases, the red curve (PV energy) gradually rises as the experiment progresses and intermittently flattens out when there is no sufficient solar production or in complete darkness. The blue curve (load energy) exhibits the same stepped behavior as expected. The battery's energy (black curve) fluctuates, increasing during charging and decreasing during discharging. A flat trend is observed for $E_{Battery}$ in all three cases during the second day, suggesting that the generated energy was not sufficient to be delivered to the load as well as stored in the battery. This behavior is in line with the previously discussed SOC progression, in which none of the scenarios involved the battery charging during the second day. The red (E_{PV}) and green (E_{MPP}), curves follow each other closely, which as previously mentioned confirms that the PV system operates very near to its maximum power point. This results in a respective energy coupling of 95.04, 95.17, 96.75 for 1,2, and 4-h battery. E_{Load} almost overlaps with E_{PV}, indicating that most of the energy produced by the PV is delivered to the load. As the battery size increases, E_{Load} shifts away from E_{PV}. This is because a larger portion of energy produced by the PV module is stored in the battery rather than transferred completely to the load and wasted whenever the intended load demand is less than the produced PV power. This is noticeable by the larger fluctuations observed for $E_{Battery}$ in the case of the 4-h battery (plot c) compared to the others. It confirms the strongest buffering effect of the larger battery, as previously mentioned, allowing better coupling.

6. Performance of the testing platform in realistic scenario

The performance of the testing platform was evaluated using data from the realistic measurement performed with the three PV-battery configurations. It consisted of assessing the capability of the testing platform to accurately reproduce the target current and voltage during the PV–battery emulation. As a result, for each configuration, the correlation between the target and the measured quantities for the current and voltage was evaluated over the measurement period. This yielded to the set of curves presented in Fig. 15 where the measured and target value of current (top row) and voltage (bottom row) are presented for 1-h battery (plots a, d), 2-h battery (plots b, e), and 4-h battery (plots c, f). The Subfigures (a), (b), and (c) show that the measured currents closely follow the target currents. In all three configurations, the points are very close to the identity line, with minor deviations, mainly visible at high amplitudes. Regarding the voltage (plots d,e,f), the platform exhibits an even higher level of accuracy. Across all PV-battery configurations, the measured voltage matches the target profile, confirming stable and accurate voltage control independent of the operating scenario.

The errors between the measured and target cumulative charge and cumulative energy during the charge and discharge phases are presented in plots (a,b,c) and (d,e,f), respectively, in Fig. 16. The comparison between measured and target cumulative charge and energy demonstrates very good agreement overall, with relative errors generally remaining small, with only 1.5%, confirming the high accuracy of the measurements. A larger deviation of about 6% is observed only for the 4-hour battery during the discharge phase. This deviation can be attributed to a charge deficiency, as the 4-hour battery did not deliver its full charge once the experiment was completed. As indicated by the corresponding energy profile (Fig. 14c), a portion of energy remained stored in the 4-hour battery at the end of the experiment. Therefore, the observed deviation could reflect incomplete discharge rather than measurement

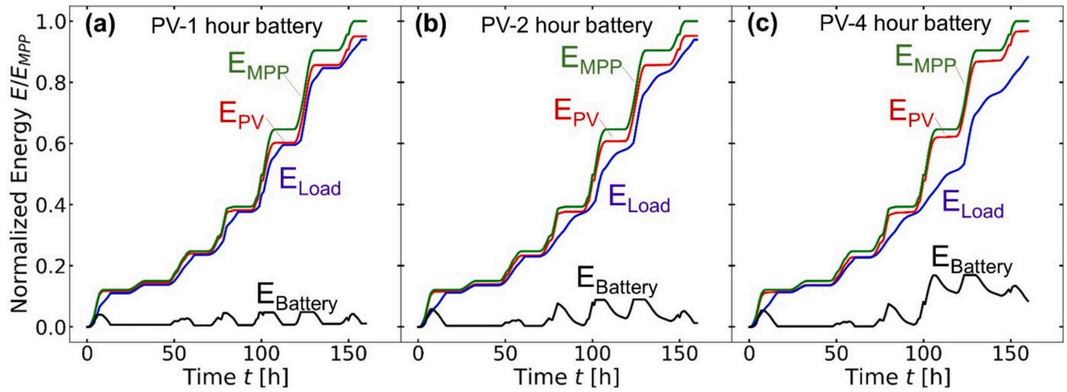

Fig. 14. Energy evolution over time in the different components of the PV-battery unit for (a) a 1-hour battery, (b) a 2-hour battery, and (c) a 4-hour battery. The plotted energies are normalized by the maximum power point energy E_{MPP}. E_{PV} (red) is the cumulative photovoltaic energy produced, E_{Load} (blue) is the cumulative energy delivered to the load, E_{Battery} (black) is the cumulative energy of the battery. (For interpretation of the references to colour in this figure legend, the reader is referred to the web version of this article.)

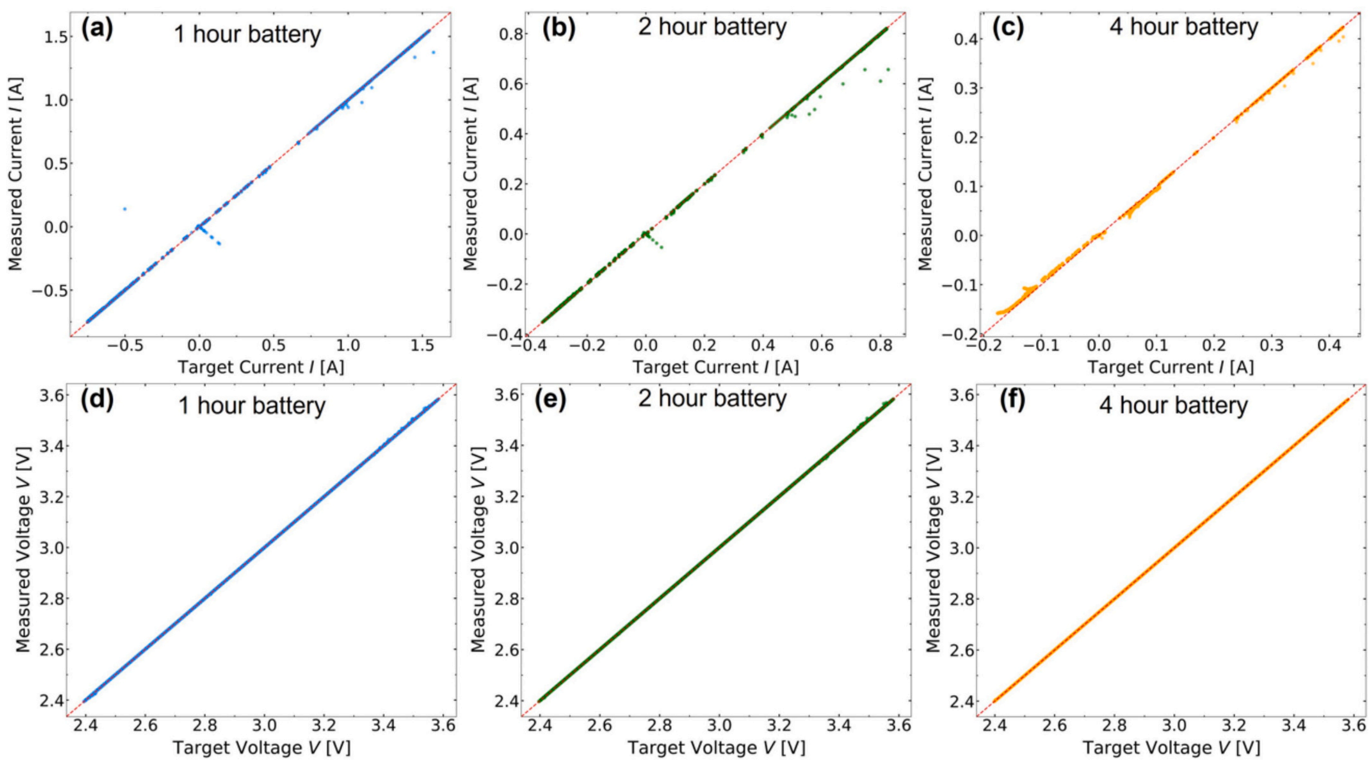

Fig. 15. Correlation plots between the measured and target values of current (top row) and voltage (bottom row) for 1-hour battery (a,d), 2-hour battery (b,e), and 4-hour battery (c,f). The red dashed line represents the ideal reference $y = x$. (For interpretation of the references to colour in this figure legend, the reader is referred to the web version of this article.)

inaccuracy.

7. Conclusion

In this work, we presented a flexible laboratory platform for testing batteries under operating conditions relevant to PV-module-level direct coupling and thermal integration. The platform combines a software-controlled PV emulator with a programmable thermal chamber, enabling batteries to be exposed to scaled PV I-V characteristics and PV-module-equivalent temperature profiles under controlled and reproducible conditions. The approach is intended to support early-stage screening of battery chemistries and cell designs before full PV-battery prototype integration.

The platform was demonstrated using a lithium-ion cell (ANR26650M1B) with a nominal voltage of 3.3 V and an operating voltage range of 2.0–3.6 V. The cell was tested as a virtual component of scaled PV-battery configurations using a representative seven-day irradiance and temperature dataset derived for a Neostar 3 N54 AIKO-A-MCE54Mw 495 W PV module in Freiburg, Germany. The emulator reproduced the target electrical conditions with cumulative charge and energy deviations of about 1.5%, while the thermal chamber followed the prescribed temperature profile with a maximum overshoot of approximately ± 1 °C. These results confirm that the platform can reproduce the selected PV-driven electrical and thermal boundary conditions with good accuracy.

Beyond platform validation, the case study illustrates how relative

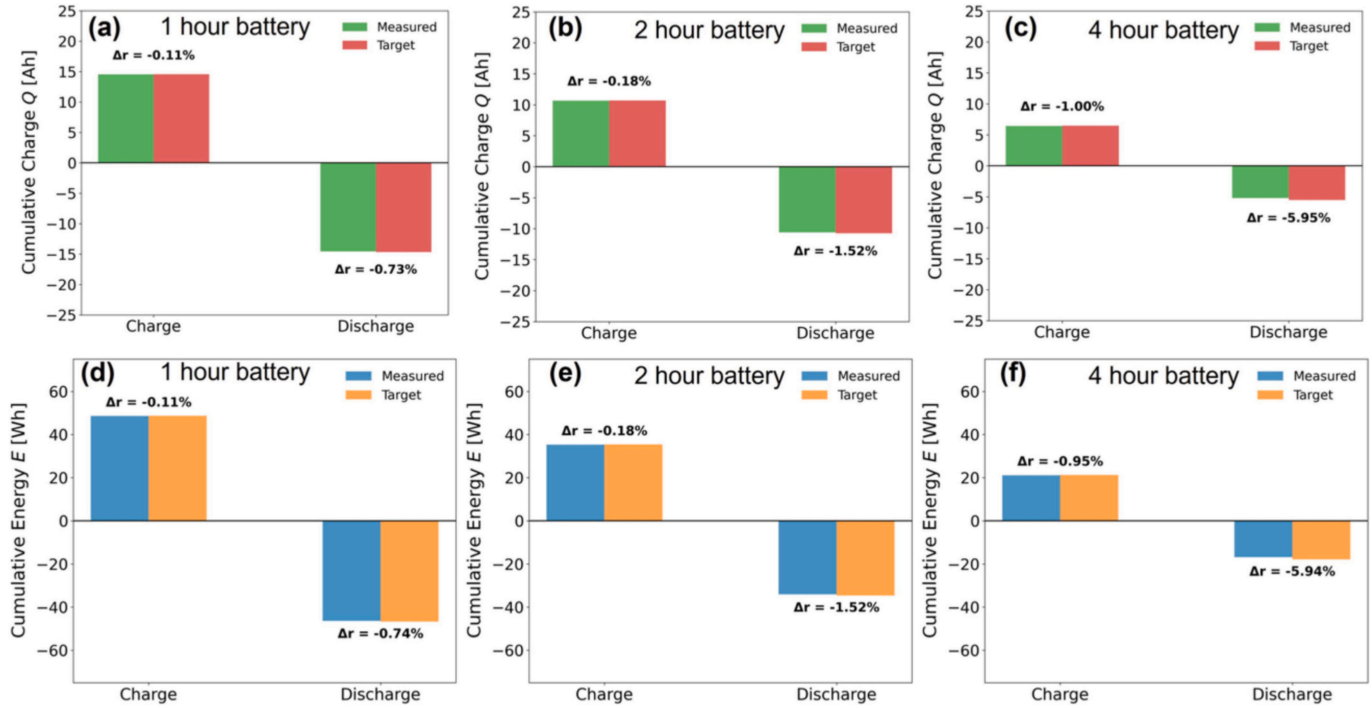

Fig. 16. Errors evaluation between the target and measured cumulative charge Q [Ah] (top row) and cumulative energy E [Wh] (bottom row) during the battery operation phases (charge and discharge) shown on the x-axis. Results are presented for the 1-hour battery (a,d), 2-hour battery (b,e), and 4-hour battery (c,f). The relative errors (Δr) between the measured and target values are indicated above each bar.

PV-battery sizing and voltage matching influence direct-coupling behavior. Smaller battery configurations experienced stronger current, voltage, and state-of-charge variations, while the tested 2-h and 4-h configurations showed more stable operation under the selected scenario. The voltage-shift experiment further showed that a 5% shift in the investigated matching condition had only a limited effect on cumulative coupling in this specific case. However, broader conclusions on optimal battery sizing or voltage-matching tolerances require additional experiments with different chemistries, voltage ranges, load profiles, climates, and ageing conditions.

The battery operating conditions obtained under the PV-driven test scenario are provided as a time series in the Supplementary Material. This dataset can be used as a simplified proxy for preliminary evaluation and comparative screening of battery chemistries on conventional battery cyclers. However, it does not reproduce the real-time PV-battery voltage feedback and I-V operating-point formation captured by the full emulation platform.

CRediT authorship contribution statement

N'Danadje Bagnabana Konga: Writing – review & editing, Writing – original draft, Visualization, Investigation, Formal analysis, Data curation. **Sergey Shcherbachenko:** Writing – review & editing, Writing – original draft, Visualization, Validation, Supervision, Software, Methodology, Formal analysis, Data curation, Conceptualization. **Oleksandr Astakhov:** Writing – review & editing, Writing – original draft, Visualization, Validation, Supervision, Methodology, Formal analysis, Conceptualization. **Daniel Weigand:** Visualization, Software, Resources, Methodology. **Ayouba Mahamane Abdoulkadri:** Writing – review & editing. **Souley Kallo Moutari:** Writing – review & editing. **Egbert Figgemeier:** Writing – review & editing, Conceptualization. **Christoph J. Brabec:** Writing – review & editing, Supervision. **Tsvetelina Merdzhanova:** Writing – review & editing, Validation, Supervision, Resources, Formal analysis, Data curation, Conceptualization.

Declaration of competing interest

The authors declare that they have no known competing financial interests or personal relationships that could have appeared to influence the work reported in this paper.

Acknowledgments

The authors acknowledge the financial support of the German Federal Ministry of Research, Technology, and Space (BMFTR) through the West African Science Service Centre on Climate Change and Adapted Land Use (WASCAL) under the International Master's Program in Energy and Green Hydrogen.

Appendix A. Supplementary data

Supplementary data to this article can be found online at https://doi.org/10.1016/j.est.2026.124007.

Data availability

Data will be made available on request.

References

[1] G. Lopez, Y. Pourjamal, C. Breyer, Paving the way towards a sustainable future or lagging behind? An ex-post analysis of the International Energy Agency's World Energy Outlook, Renew. Sust. Energ. Rev. 212 (2025) 115371, https://doi.org/10.1016/j.rser.2025.115371.

[2] M. Ram, D. Bogdanov, A. Aghahosseini, A. Gulagi, S.A. Oyewo, M. Child, U. Caldera, K. Sadovskaia, J. Farfan, L.S.N.S. Barbosa, M. Fasihi, S. Khalili, C. Breyer, H.-J. Fell, Energy Transition in Europe Across Power, Heat, Transport and Desalination Sectors, 2018, https://doi.org/10.13140/RG.2.2.10143.00160.

[3] D. Heide, L. Von Bremen, M. Greiner, C. Hoffmann, M. Speckmann, S. Bofinger, Seasonal optimal mix of wind and solar power in a future, highly renewable Europe, Renew. Energy 35 (2010) 2483–2489.

[4] Optimal Integration of PV in Micro-grids Dominated by Diesel Power Plants, IEA PVPS, 2019. https://iea-pvps.org/key-topics/optimal-integration-of-photovoltaic

s-in-micro-grids-that-are-dominated-by-diesel-power-plants/ (accessed June 24, 2026).
[5] Z. Zhu, T. Jiang, M. Ali, Y. Meng, Y. Jin, Y. Cui, W. Chen, Rechargeable batteries for grid scale energy storage, Chem. Rev. 122 (2022) 16610–16751.
[6] Z. Dong, Y. Tao, S. Lai, T. Wang, Z. Zhang, Powering future advancements and applications of battery energy storage systems across different scales, Energy Storage Appl. 2 (2025) 1.
[7] Z. Chen, T. Wang, F. Wang, What's hindering the deployment of energy storage devices in distributed photovoltaic systems: an evolutionary game analysis based on system dynamics, J. Renew. Sustain. Energy 16 (2024).
[8] G.N. Psarros, P.A. Dratsas, P.P. Chinaris, S.A. Papathanassiou, Assessing the implications of RES technology mix on curtailments, storage requirements and system economics, Appl. Energy 381 (2025) 125159.
[9] D. Newbery, C.E.P.R. Group, et al., Implications of renewable electricity curtailment for delivered costs, Energy Econ. 145 (2025) 108472.
[10] T. Su, J. Zhao, A. Gomez-Exposito, Y. Chen, V. Terzija, J.P. Gentle, Grid-enhancing technologies for clean energy systems, Nat. Rev. Clean Technol. 1 (2025) 16–31.
[11] M. Laimon, Renewable energy curtailment: a problem or an opportunity? Results Eng. 26 (2025) 104925.
[12] O. Astakhov, T. Merdzhanova, L. Kin, U. Rau, From room to roof: how feasible is direct coupling of solar-battery power unit under variable irradiance ? Sol. Energy 206 (2020) 732–740, https://doi.org/10.1016/j.solener.2020.06.033.
[13] S. Shcherbachenko, O. Astakhov, U. Chime, L.C. Kin, K. Ding, B. Pieters, U. Rau, E. Figgemeier, T. Merdzhanova, Efficient power coupling in directly connected photovoltaic-battery module, Sol. RRL 7 (2023), https://doi.org/10.1002/solr.202200857.
[14] S.N. Agbo, T. Merdzhanova, S. Yu, H. Tempel, H. Kungl, R. Eichel, U. Rau, O. Astakhov, Development towards cell-to-cell monolithic integration of a thin-film solar cell and lithium-ion accumulator, J. Power Sources 327 (2016) 340–344, https://doi.org/10.1016/j.jpowsour.2016.07.073.
[15] F. Sandbaumhüter, S.N. Agbo, C. Tsai, O. Astakhov, S. Uhlenbruck, U. Rau, T. Merdzhanova, Compatibility study towards monolithic self-charging power unit based on all-solid thin- film solar module and battery, J. Power Sources 365 (2017) 303–307, https://doi.org/10.1016/j.jpowsour.2017.08.103.
[16] U. Chibuko, T. Merdzhanova, D. Weigand, F. Ezema, S. Agbo, U. Rau, O. Astakhov, Module-level direct coupling in PV-battery power unit under realistic irradiance and load, Sol. Energy 249 (2023) 233–241, https://doi.org/10.1016/j.solener.2022.11.040.
[17] N. Kakimoto, R. Asano, Linear operation of photovoltaic array with directly connected lithium-ion batteries, IEEE Trans. Sustain. Energy 8 (2017) 1647–1657.
[18] S.P. Ayeng'o, H. Axelsen, D. Haberschusz, D.U. Sauer, A model for direct-coupled PV systems with batteries depending on solar radiation, temperature and number of serial connected PV cells, Sol. Energy 183 (2019) 120–131.
[19] V. Leible, W.G. Bessler, Passive hybridization of photovoltaic cells with a lithium-ion battery cell: an experimental proof of concept, J. Power Sources 482 (2021) 229050.
[20] R. Behmann, J. Phan, A. Root, M. Schmidt, W.G. Bessler, Integration of a lithium-ion battery in a micro-photovoltaic system: passive versus active coupling architectures, Sol. Energy 262 (2023) 111748.
[21] M. Hasan, A.H. Sabry, H. Serra Altinoluk, Maximizing energy transfer of solar-battery charge controller using voltage balancing strategy, Results Eng. 23 (2024) 102604, https://doi.org/10.1016/j.rineng.2024.102604.
[22] A.H. Sabry, W.Z.W. Hasan, M.A. Kadir, M.a.M. Radzi, S. Shafie, DC-based smart PV-powered home energy management system based on voltage matching and RF module, PLoS One 12 (2017) e0185012, https://doi.org/10.1371/journal.pone.0185012.
[23] Y. Kanai, F. Kurokawa, Evaluation of passive maximum power point tracking performance of power conditioner-less PV-storage battery systems, in: 2025 14th International Conference on Renewable Energy Research and Applications (ICRERA), 2025, pp. 1089–1093, https://doi.org/10.1109/ICRERA66237.2025.11284265.
[24] V. Vega-Garita, L. Ramirez-Elizondo, P. Bauer, Physical integration of a photovoltaic-battery system: a thermal analysis, Appl. Energy 208 (2017) 446–455.
[25] M. Hammami, S. Torretti, F. Grimaccia, G. Grandi, Thermal and performance analysis of a photovoltaic module with an integrated energy storage system, Appl. Sci. 7 (2017) 1107.
[26] M. Schweiger, J. Bonilla, W. Herrmann, A. Gerber, U. Rau, Performance stability of photovoltaic modules in different climates, Prog. Photovolt. Res. Appl. 25 (2017) 968–981.
[27] A. von Jouanne, E. Agamloh, A. Yokochi, Power Hardware-in-the-Loop (PHIL): a review to advance smart inverter-based grid-edge solutions, Energies 16 (2023) 916, https://doi.org/10.3390/en16020916.
[28] C. Caruana, A. Sattar, A. Al-Durra, S.M. Muyeen, Real-time testing of energy storage systems in renewable energy applications, Sustain. Energy Technol. Assess. 12 (2015) 1–9, https://doi.org/10.1016/j.seta.2015.08.001.
[29] J. Khazaei, L. Piyasinghe, V.R. Disfani, Z. Miao, L. Fan, G. Gurlaskie, Real-time simulation and hardware-in-the-loop tests of a battery system, in: 2015 IEEE Power & Energy Society General Meeting, 2015, pp. 1–5, https://doi.org/10.1109/PESGM.2015.7285993.
[30] J. Kumar, M. Mekkanen, M. Karimi, K. Kauhaniemi, Hardware-in-the-loop testing of a battery energy storage controller for harbour area smart grid: a case study for Vaasa harbour grid, Energy Rep. 9 (2023) 447–454, https://doi.org/10.1016/j.egyr.2023.01.068.
[31] H. Haupt, M. Plöger, J. Bracker, Hardware-in-the-loop test of battery management systems, IFAC Proc. Vol. 46 (2013) 658–664, https://doi.org/10.3182/20130904-4-JP-2042.00042.
[32] M.F. Seidler, B. Pieters, W. Zwaygardt, S. Haas, O. Astakhov, T. Merdzhanova, A photovoltaics emulator for electrochemistry using Python and SCPI, J. Power Sources 641 (2025) 236723.
[33] D. Faiman, Assessing the outdoor operating temperature of photovoltaic modules, Prog. Photovolt. Res. Appl. 16 (2008) 307–315.
[34] W. Goodfriend, E.B. Pieters, M. Tsvetelina, A. Solomon, F. Ezema, U. Rau, Development and improvement of a transient temperature model of PV modules: concept of trailing data, Prog. Photovolt. Res. Appl. 32 (2024) 399–405.
[35] S. Uprety, H. Lee, 23.6 A 43V 400mW-to-21W global-search-based photovoltaic energy harvester with 350μs transient time, 99.9% MPPT efficiency, and 94% power efficiency, in: 2014 IEEE International Solid-state Circuits Conference Digest of Technical Papers (ISSCC), 2014, pp. 404–405.
[36] S. Uprety, H. Lee, 22.5 A 93%-power-efficiency photovoltaic energy harvester with irradiance-aware auto-reconfigurable MPPT scheme achieving> 95% MPPT efficiency across 650μW to 1W and 2.9 ms FOCV MPPT transient time, in: 2017 IEEE International Solid-State Circuits Conference (ISSCC), 2017, pp. 378–379.